Boosting Electrochemical Oxygen Reduction Performance of Iron Phthalocyanine through Axial Coordination Sphere Interaction

Zhang, W.; Meeus, E.J.; Wang, L.; Zhang, L.H.; Yang, S.; de Bruin, B.; Reek, J.N.H.; Yu, F.

DOI
10.1002/cssc.202102379

Publication date
2022

Document Version
Final published version

Published in
ChemSusChem

ChemSusChem

Research Article
doi.org/10.1002/cssc.202102379

Chemistry Europe
European Chemical Societies Publishing

www.chemsuschem.org

Boosting Electrochemical Oxygen Reduction Performance of Iron Phthalocyanine through Axial Coordination Sphere Interaction

Wenlin Zhang[+],[a] Eva J. Meeus[+],[b] Lei Wang,[a] Lu-Hua Zhang,*[a] Shuangcheng Yang,[a] Bas de Bruin,*[b] Joost N. H. Reek,[b] and Fengshou Yu*[a]

Precise regulation of the electronic states of catalytic sites through molecular engineering is highly desired to boost catalytic performance. Herein, a facile strategy was developed to synthesize efficient oxygen reduction reaction (ORR) catalysts, based on mononuclear iron phthalocyanine supported on commercially available multi-walled carbon nanotubes that contain electron-donating functional groups (FePc/CNT-R, with "R" being $-NH_2$, –OH, or –COOH). These functional groups acted as axial ligands that coordinated to the Fe site, confirmed by X-ray photoelectron spectroscopy and synchrotron-radiation-based X-ray absorption fine structure. Experimental results showed that FePc/CNT-NH_2, with the most electron-donating $-NH_2$ axial ligand, exhibited the highest ORR activity with a positive onset potential (E_{onset} = 1.0 V vs. reversible hydrogen electrode) and half-wave potential ($E_{1/2}$ = 0.92 V). This was better than the state-of-the-art Pt/C catalyst (E_{onset} = 1.00 V and $E_{1/2}$ = 0.85 V) under the same conditions. Overall, the functionalized FePc/CNT-R assemblies showed enhanced ORR performance in comparison to the non-functionalized FePc/CNT assembly. The origin of this behavior was investigated using density functional theory calculations, which demonstrated that the coordination of electron-donating groups to FePc facilitated the adsorption and activation of oxygen. This study not only demonstrates a series of advanced ORR electrocatalysts, but also introduces a feasible strategy for the rational design of highly active electrocatalysts for other proton-coupled electron transfer reactions.

Introduction

The oxygen reduction reaction (ORR) lies at the heart of several renewable-energy conversion devices, such as fuel cells and metal-air batteries, but generally suffers from sluggish kinetics and large overpotentials.[1] Although Pt-based materials are still the most effective ORR catalysts to date,[2] pursuing non-precious metal catalysts with superior performance over Pt-based materials is highly desirable considering the unaffordable price and scarce resources of platinum.[3] Metal-N_4 macrocyclic compounds based on non-precious transition metals, including porphyrins and phthalocyanines, have been extensively studied as ORR catalysts.[4] Especially iron phthalocyanine (FePc), which is based on a tetracoordinate planar Fe–N_4 center, has gained significant attention because of its good ORR activity.[5] The typical Fe–N_4 configuration in FePc is located at the left of the volcano-type plot for ORR, which indicates a rather strong binding with the reaction intermediates.[6] Based on the Sabatier principle, a catalyst is ideally located at the apex of a volcano-type plot, since moderate binding strength (neither too strong nor too weak) with reaction intermediates typically results in the best catalytic performance.[6b,7] Optimizing the binding strength of the reaction intermediates on the Fe–N_4 active site is therefore essential for the enhancement of the ORR performance of FePc.[8]

Synthetic macrocyclic complexes active in ORR, such as FePc, typically have a planar and symmetric structure. Cytochrome *c* oxidase, an efficient ORR catalyst present in the respiratory chain, contains a Fe-porphyrin site and a bimetallic copper cofactor.[9] Interestingly, the Fe-porphyrin site has a five-coordinated configuration bearing an axial ligand. This axial coordination to the Fe site tends to increase electron density on the Fe site, which is favorable for O_2 binding and facilitates the O–O bond cleavage, which leads to an improved ORR performance.[10] Inspired by the axial coordination strategy, a series of synthetic electron regulation strategies, based on axial coordination, have been employed to optimize the catalytic performance of Fe–N_4 based catalysts.[4a,11] However, such homogeneous catalytic systems typically require complex organic synthesis routes to enable molecularly precise manipulation of the coordination environments of the active sites.[4a,11a,12] Additionally, homogeneous systems generally suffer from sluggish diffusion to the electrode surface.[4a,13] Non-covalent heterogenization of molecular catalysts onto highly conductive electrodes, such as a carbon materials, is an effective way to address the above obstacles from their practical

[a] Prof. W. Zhang,[+] L. Wang, Dr. L.-H. Zhang, S. Yang, Dr. F. Yu
National-Local Joint Engineering Laboratory for Energy Conservation in Chemical Process Integration and Resources Utilization
School of Chemical Engineering and Technology
Hebei University of Technology
Tianjin 300130 (P. R. China)
E-mail: luhuazhang@hebut.edu.cn
yfsh@hebut.edu.cn

[b] E. J. Meeus,[+] Prof. B. de Bruin, Prof. J. N. H. Reek
Van 't Hoff Institute for Molecular Sciences
University of Amsterdam
Science Park 904, 1098 XH Amsterdam (The Netherlands)
E-mail: b.debruin@uva.nl

[+] These authors contributed equally to this work.

Supporting information for this article is available on the WWW under https://doi.org/10.1002/cssc.202102379

applications.[8b,11b,14] Along this line, metal-N_4 macrocyclic molecular catalysts have been anchored on electrodes through weak interactions such as π-π stacking.[8b] Interestingly, for these heterogenization cases, the defects of the support can induce electronic localization of the catalytic site, which regulates O_2 adsorption and activation, and thus the ORR performance.[8b,13,15] Furthermore, experimental and theoretical studies have revealed that the electron-donating property (electronegativity) of functional groups that are axially coordinated play an important role on electron regulation of the active sites, which in turn contributes to the ORR activity.[11b,16] However, a direct experimental evaluation of the effect of the electron-donating properties of axial ligands on the ORR activity of Fe–N_4 based catalysts is often difficult for noncovalent heterogenization cases. This is mostly due to the differences in chemical properties among supports, as a result of e.g. surface morphology and pore structure, which can influence the ORR activity. Carbon nanotubes (CNTs) are widely utilized as electrocatalytic supports due to their high mechanical strength, good thermal stability, and strong conductivity. Additionally, CNTs possess porous structure, which not only facilitates the transport of substance, but also has electron interactions with the active phase of the catalyst. The easily accessible and tunable functional groups on the surface of CNTs could lead to a high surface energy and tunable chemisorption ability, thus favorable for interactions with active sites.[17]

Hence, the focus of our work is to develop a series of hybrid electrocatalysts, through a self-assembly strategy, which preferably only differ in the respective functional groups of the electrode matrix. Specifically, using commercially functionalized multi-walled carbon nanotubes (CNT-R, where "R" represents the functional groups including –NH_2, –OH, and –COOH) as design platforms, we investigated the influence of the electron-donating ability of these functional groups, which serve as axial ligands coordinated to the Fe site of FePc, on the ORR activity. Experimental results show that the coordination of electron-donating axial ligands to FePc via functionalized CNTs boosts the ORR activity. The FePc/CNT-NH_2 catalyst exhibited the highest ORR activity with a positive onset potential [E_{onset} = 1.0 V vs. reversible hydrogen electrode (RHE)] and half-wave potential ($E_{1/2}$ = 0.92 V), which is better than the most advanced Fe-based ORR catalysts and the state-of-the-art Pt/C catalyst (E_{onset} = 1.00 V and $E_{1/2}$ = 0.85 V) under the same conditions. Density functional theory (DFT)-based calculations revealed that the axial coordination of electron donating ligands facilitates the adsorption of O_2. Moreover, the formation of the rate determining reaction intermediates, such as OOH*, turns out to be less endothermic for the functionalized catalysts, which is reflected in the lower overpotentials required for the ORR.

Results and Discussion

The FePc/CNT-R catalysts were prepared via the dropwise addition of a homogeneous DMF solution of FePc into a suspension of CNT-R. The anchoring of FePc onto the matrix typically involves π-π stacking interactions and is enhanced by the interactions between the electron-rich functional groups that coordinate to the electron-deficient Fe-site of FePc. The following assemblies were successfully synthesized and characterized: FePc/CNT, FePc/CNT-COOH, FePc/CNT-OH, and FePc/CNT-NH_2 (Figure 1a). With the help of scanning electron microscopy (SEM, Figure S1) and transmission electron microscopy (TEM) the compositions of the FePc/CNT-R assemblies were confirmed to be consistent with the initial and typical tubular morphology of CNT-R (Figures 1b,c and S2). After the self-assembly, FePc loading onto CNT-R was first demonstrated by the characteristic vibrations of the Fourier-transform infrared (FTIR) spectra (Figure S3). The uniform distribution of FePc on CNT-R was confirmed with energy-dispersive X-ray spectroscopy (EDS) mapping, which clearly display a homogeneous distribution of C, N, and Fe elements (Figure 1d). Moreover, X-ray diffraction (XRD) patterns (Figure S4) of all samples show two broad peaks, assigned to the (002) and (101) planes of carbon. No diffraction peaks related to FePc are identified. Specifically, in comparison to bare CNT-R, the characteristic peaks of the (002) planes of all the assemblies reveal slight shifts to a higher angle. This observation is indicative for π-π interactions between FePc and the CNT-R supports (Figure S4).[8b] This is further supported by the obtained Raman spectra of the assemblies. The Raman spectrum of the bare CNT shows two typical peaks: the D band (1341 cm^{-1}) and G band (1581 cm^{-1}), that are attributed to the disordered, defective, and crystalline graphite bands respectively. For all FePc/CNT-R assemblies, however, the D band is separated into two bands (1340 and 1297 cm^{-1}) and the G band at 1581 cm^{-1} has progressively

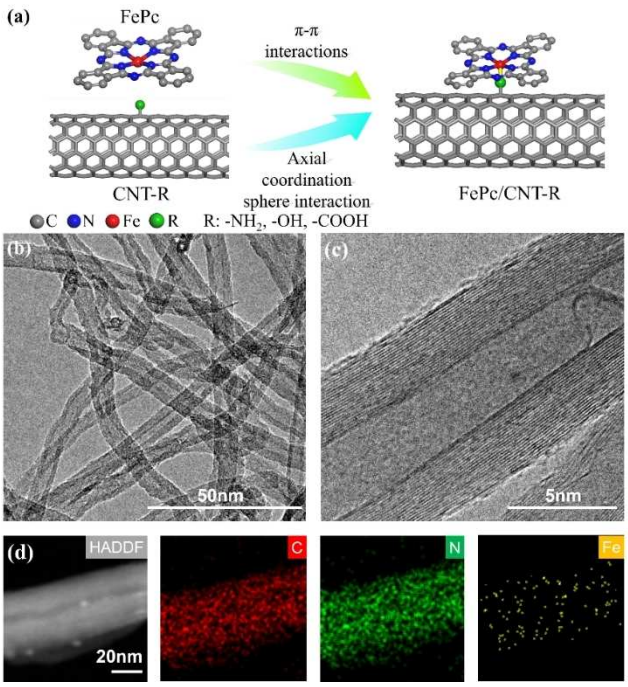

Figure 1. (a) Schematic representation of the self-assembly process of the FePc/CNT-R catalyst. (b,c) TEM image of FePc/CNT-NH_2. (d) High-angle annular dark-field (HADDF) image and the corresponding EDS mapping for C, N, and Fe elements of FePc/CNT-NH_2.

shifted to 1595 cm^{-1} (Figure S5). These changes in Raman bands have previously been reported to be directly correlated with the non-planar distortion of phthalocyanine complexes induced by π-π stacking.[17] The loadings of FePc in FePc/CNT-NH_2, FePc/CNT-OH, and FePc/CNT-COOH were 2.96, 2.53, and 2.38%, respectively, determined by the inductively coupled plasma (ICP) analysis.

To obtain insight into the elemental states on the surface of the assemblies, high-resolution X-ray photoelectron spectroscopy (XPS) spectra were collected. The elemental surveys for all assemblies reveal the presence of the C 1s, N 1s, O 1s, and Fe 2p without any other element present (Figure S6). The high-resolution spectra measured for Fe, show two peaks at 710.8 and 723.8 eV that correspond to Fe $2p_{3/2}$ and Fe $2p_{1/2}$ in FePc (Figure S7). Moreover, distinct signals characteristic for Fe–N and Fe–O bonds were detected for FePc/CNT-NH_2, FePc/CNT-OH and FePc/CNT-COOH respectively (Figure 2a), confirming axial coordination of N and O atoms. For the O 1s high-resolution spectra, the fitted ratio of Fe–O bonds in FePc/CNT-OH and FePc/CNT-COOH samples, are significantly higher when compared to the spectrum of FePc/CNT. This indicates the axial coordination of an oxygen atom to the Fe–N_4 sites (Figure 2b).[18] The N 1s high-resolution spectrum of FePc/CNT can be deconvoluted into two main peaks at 397.9 and 399.2 eV, corresponding to C–N and Fe–N bonds (Figure 2c). The fitted ratio of the Fe–N bond in FePc/CNT-NH_2 shows a significant increase when compared to FePc/CNT, FePc/CNT-OH, and FePc/CNT-COOH. This result is thus indicative for an Fe–N bond in FePc/CNT-NH_2, resulting from axial coordination of the –NH_2 functionalized CNT.

In order to further investigate the coordination environment of the Fe site, synchrotron-radiation-based X-ray absorption fine structure [XAFS, composed of X-ray absorption near-edge structure (XANES) and extended X-ray absorption fine structure (EXAFS)] measurements were conducted with Fe and Fe_2O_3 as reference. For XANES analysis, the shoulder peak of FePc in the Fe K-edge (Figure 2d) at 7111 eV can be attributed to the square planar and centrosymmetric Fe–N_4 structure (D_{4h} symmetry) resulting from the 1 s→4 p_z conversion.[13,19] The shoulder shifts to 7112 eV for Fe–Pc/CNT-R. This indicates a significant change in the local symmetry of Fe–N_4, that is likely induced by the additional coordination of OH or NH_2 with Fe.[15] For the Fe K-edge Fourier-transform (FT) EXAFS, the position of the FT peak shifts from 1.50 Å for FePc to 1.53 Å for FePc/CNT-OH and FePc/CNT-COOH. For FePc/CNT-NH_2 (Figure 2e), the shift is even more significant with 1.60 Å. These shifts suggest different coordination environments.[20] The fine coordination environment of the Fe atoms was further analyzed by EXAFS curve-fitting, which revealed additional Fe–N or Fe–O coordination bonds for FePc/CNT-R in comparison to FePc/CNT, as well. Moreover, the fitting curves are in good agreement with the experimentally obtained spectra (Figures 2f, S8, and Table S1). All the above results confirm the existence of N–FeN_4 bonds in FePc/CNT-NH_2 and O–FeN_4 bonds in FePc/CNT-COOH and FePc/CNT-OH, respectively.

In order to probe the change of electron states after loading FePc to CNT-R, temperature-dependent magnetic susceptibility (M–T) measurements (Figure S9a,b) and electron paramagnetic resonance (EPR) spectroscopy (Figure S9c,d) were performed for FePc and FePc/CNT-NH_2. From the 1/χ (χ stands for magnetic

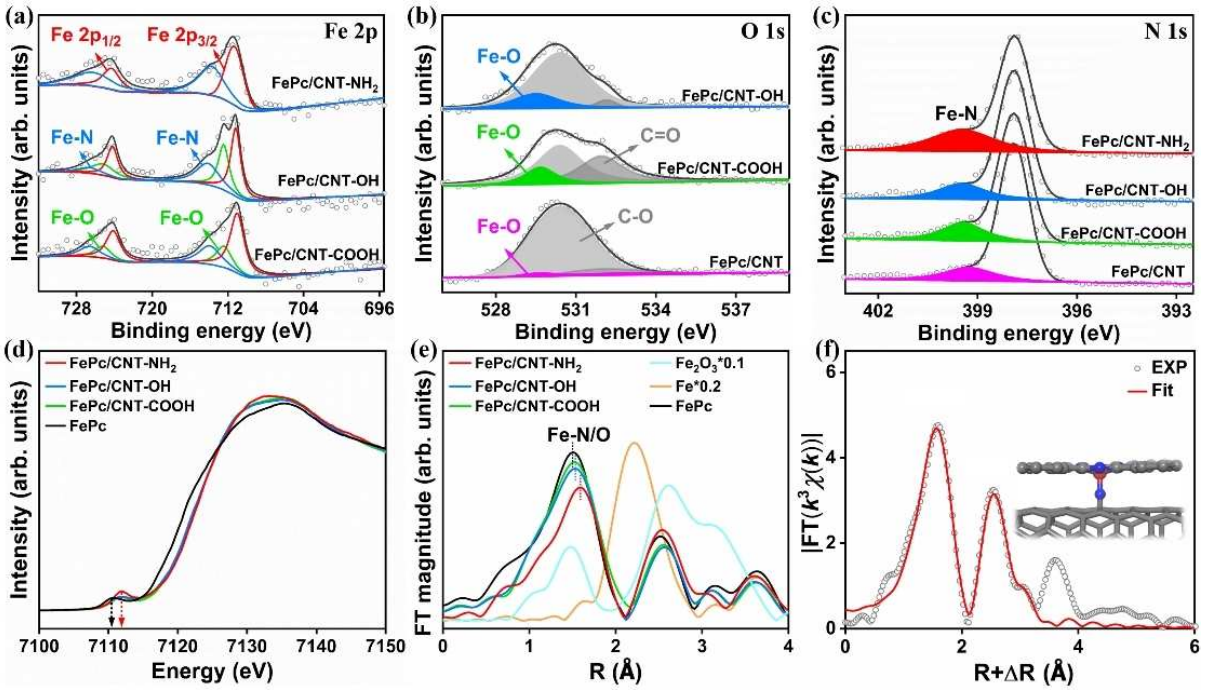

Figure 2. (a) Fe 2p XPS spectra of FePc/CNT-R. (b) O 1s XPS spectra of FePc/CNT-OH, FePc/CNT-COOH, and FePc/CNT. (c) N 1s XPS spectra of FePc/CNT and FePc/CNT-R. (d) XANES spectra at the Fe K-edge of FePc/CNT-R and FePc. (e) k^3-weighted Fourier transforms of the EXAFS spectra of FePc/CNT-R, Fe foil, Fe_2O_3 and FePc. (f) Fitting of k^3-weighted Fe K-edge EXAFS for FePc/CNT-NH_2.

moment per unit mass) plot (Figure S9b), it can be seen that the paramagnetic state is greatly weakened after loading FePc to CNT-NH_2 compared to FePc. This indicates that less free electrons with Pauli paramagnetism travel around the Fe^{II} center.[5a] While in the EPR spectra, it shows an obvious *g* factor shift from 1.99034 to 1.99205 after loading to CNT-NH_2, which suggests that the unpaired electrons around the central Fe atom increased.[21] The additionally coordination sphere was confirmed to be beneficial for oxygen adsorption by O_2 temperature-programmed desorption (TPD, Figure S10).[22]

To characterize the ORR performance of FePc/CNT-R, linear sweep voltammetry (LSV) was carried out using a rotating disk electrode (RDE) set-up. Remarkably, E_{onest} and $E_{1/2}$ of FePc/CNT-NH_2 reach 1.00 V and 0.92 V, respectively, which is a significant improvement in comparison to unsupported FePc (E_{onset} = 0.83 V and $E_{1/2}$ = 0.75 V), demonstrating the positive effect of heterogenization. Moreover, the ORR catalytic potentials of FePc/CNT-NH_2 are superior over the state-of-the-art Pt/C catalyst (E_{onest} = 1.00 V and $E_{1/2}$ = 0.85 V) and outstanding when compared with the most advanced and recently reported single Fe site catalysts (Table S2).[5,6a,8b,13,15,23] Furthermore, all FePc/CNT-R assemblies, where axial coordination to FePc is present, show a more positive E_{onest} and $E_{1/2}$ compared to FePc/CNT. The degree of this shift, towards a more positive value, is in the order of FePc/CNT-NH_2 (E_{onest} = 1.00 V and $E_{1/2}$ = 0.92 V) > FePc/CNT-OH (E_{onset} = 0.98 V and $E_{1/2}$ = 0.89 V) > FePc/CNT-COOH (E_{onset} = 0.96 V and $E_{1/2}$ = 0.87 V) > FePc/CNT (E_{onest} = 0.93 V and $E_{1/2}$ = 0.85 V). This trend illustrates that axial coordination of more electron-donating groups enhances the ORR activity for the FePc/CNT-R assemblies, with the FePc/CNT-NH_2 catalyst demonstrating the highest activity. In addition, FePc/CNT-NH_2 shows an impressive kinetic current density of 8.5 mA cm^{-2}, which is three times more than that of Pt/C catalyst (J_k = 2.8 mA cm^{-2}).[5a,24] Similar to the observed trend in potentials, the kinetic current density of all the catalysts with axial coordination is significantly higher than that of FePc/CNT (Figure 3c). The catalytic activity was normalized by the loading of FePc on CNT-R and we found that FePc/CNT-NH_2 still had the highest activity for the ORR (Table S3). Furthermore, electrochemical impedance spectroscopy (EIS) was used to characterize the impedance of all catalysts (Figure S11). FePc/CNT-NH_2 shows the smallest impedance (FePc/CNT-NH_2 < FePc/CNT-OH < FePc/CNT-COOH < FePc/CNT) which is consistent with the trends in kinetic current density and potentials. Besides the kinetic current density and catalytic potentials, the Tafel slope is a sufficient reflection of the catalytic activity as well. Among all samples, FePc/CNT-NH_2 exhibits the lowest Tafel slope of 44.3 mV dec^{-1}, indicating a fast kinetic process for ORR (Figure 3d).

To further understand the catalytic process, the average electron transfer number (*n*) for all assemblies during ORR was determined from the Koutecky-Levich (K-L) equation (Figure S12). The value of *n* is up to 4.04 for FePc/CNT-NH_2, indicating that the ORR process proceeds via a typical four-electron transfer pathway (Figure S13). The other two functionalized assemblies show a larger *n* (4.02 for FePc/CNT-OH and 3.99 for FePc/CNT-COOH), than the unfunctionalized FePc/CNT assembly (3.97). Rotating ring disk electrode (RRDE) experiments were performed to further investigate the electron-transfer and selective formation of H_2O over H_2O_2 experimentally (Figure S14 and Figure 3e). In comparison to the other three composite catalysts, FePc/CNT-NH_2 shows an increased

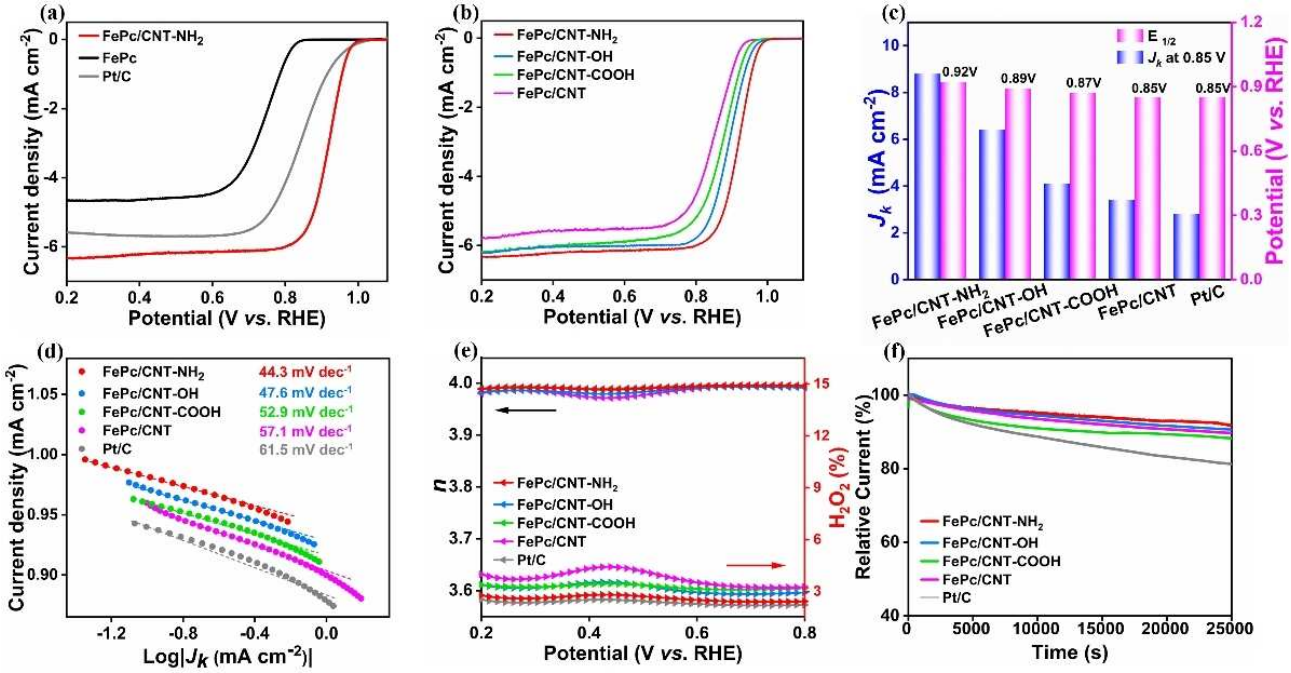

Figure 3. (a) LSV curves of FePc, FePc/CNT-NH_2, and Pt/C in 0.1 M KOH. (b) LSV curves of FePc/CNT and FePc/CNT-R. (c) Half-wave potential and kinetic current density (J_k). (d) Tafel slope. (e) Electron transfer number and H_2O_2 yield, and (f) stability curves test in 0.1 M KOH of FePc/CNT, FePc/CNT-R, and Pt/C.

electron transfer and the lowest selectivity for H_2O_2 production. This supports the proposed fast and facile kinetic process for O_2 activation on the functionalized catalyst.

To explore the practical application of FePc/CNT-NH_2, the long-term catalytic stability and tolerance towards methanol were examined. As shown in Figure 3f, 92% of the relative current remains for FePc/CNT-NH_2 after 25000 s chronoamperometric *i-t* testing, exceeding that of Pt/C (81% of the relative current remains under similar conditions). In addition, no obvious current oscillation was observed for FePc/CNT-NH_2 when methanol was added, whereas for Pt/C a clear decline of current was observed (Figure S15). The above results indicate an excellent stability and resistance towards methanol poisoning for FePc/CNT-NH_2.

In accordance with the previously discussed results, the axial coordination of electron-donating ligands via functionalized CNTs can greatly boost the ORR performance of FePc. To gain more insight into the effect of axial ligand coordination on the catalytic performance of the experimentally examined ORR catalysts, theoretical investigations have been carried out with DFT (see computational details in the Supporting Information). Since we focused on the effect of different axially coordinated electron donating ligands on the ORR activity, we used a simplified model system for the FePc/CNT-R catalysts: FePc/Ar-R (see computational details, Figure S16). Herein, "Ar" represents an aryl group and "R" the functional group of the axial ligand donors. FePc is used as a reference compound.

The proposed five-step mechanism for ORR with the FePc/CNT-R catalysts is shown in Figure 4a for FePc/Ar–NH_2. In line with the experimentally determined average electron transfer number, the ORR proceeds via an associative four electron pathway in which O_2 is reduced to two H_2O molecules in a stepwise manner. Initially, O_2 adsorbs (coordinates) on the Fe site in an end-on fashion forming the first intermediate: O_2*. The experimentally observed trend in the O_2 adsorption ability of the catalysts is in agreement with the computed more stabilizing formation enthalpy of the FePc-O_2/Ar–R complexes (−0.660 to −0.633 eV) in comparison to the FePc-O_2 complex without axial coordination (−0.613 eV, Table S8). This trend likely results from the electron donating abilities of the axial ligands. Their coordination increases the electron density at the Fe site and hence facilitate oxygen adsorption (more exergonic overall O_2-binding). Due to the reduction of O_2 upon binding to the Fe site, the O–O bond length is significantly elongated (

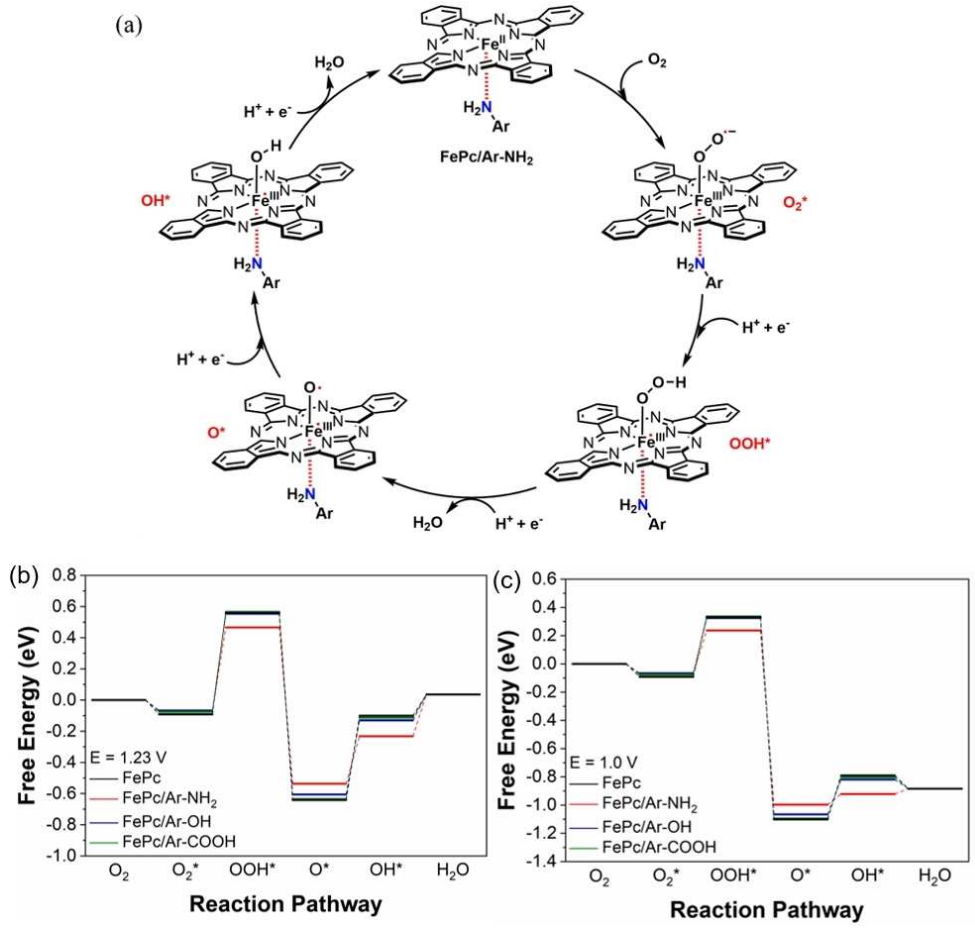

Figure 4. (a) Proposed mechanism for ORR on FePc/CNTs via an associative four-electron pathway, yielding two molecules of H_2O, shown for FePc/Ar–NH_2. Free-energy diagram for complete O_2 reduction on the FePc and FePc/Ar-R model catalysts at (b) $E = 1.23$ V (0 mV overpotential) and (c) $E = 1.0$ V (230 mV overpotential) vs. RHE in alkaline medium.

≈1.27 Å) upon adsorption on all catalysts in comparison to unbound O_2 (1.218 Å, Table S9). Moreover, another trend among the different complexes can be observed in the first reaction step. Namely, FePc–O_2 displays the shortest Fe–O bond length (1.728 Å) while the functionalized catalysts show elongated Fe–O bonds, for example, FePc-O_2/Ar–NH_2 (1.761 Å, Table S9). During this first step, the adsorption of dioxygen results in the formation of a Fe^{III}-superoxide intermediate. Axial coordination of electron donating groups results in a longer Fe–O bond of the superoxide ligand, due to competing orbital overlap and a higher electron density at iron, affecting the sigma-bond between Fe^{III} and the superoxide ligand. This is a manifestation of the *trans*-influence of the axial coordinated ligands and is also clearly visible in the other ORR steps.

After the formation of the O_2* intermediate, proton-coupled electron transfer (PCET) on the farther oxygen atom results in the formation of the OOH* intermediate. Consequently, the O–O bond becomes even more elongated and resembles a bond length characteristic for a single bond (FePc/Ar–NH_2: 1.455 Å, Table S9). Furthermore, the FePc–OOH complex shows a significantly shorter Fe–O bond (1.758 Å) than the other FePc/Ar–R catalysts, with FePc–OOH/Ar–NH_2 displaying the longest bond (1.791 Å, Table S9). Ultimately, two water molecules are formed via two consecutive PCET steps, that display a similar trend in the elongation of the Fe–O bond length (Table S9).

To sum up the above-mentioned results, the calculated trends in formation enthalpy, in addition to the observed trends in elongated Fe–O bond lengths, clearly demonstrate the effect of the axial coordination of electron donating groups. Since these trends relate to the electron donating capacity of the axial ligands, a natural population analysis (NPA) was performed for all ORR intermediates (Figure S17).[25] The development of NPA charges demonstrates a decrease in positive charge on the Fe sites for the functionalized FePc catalysts (e.g., FePc/Ar–NH_2: +0.96234), with respect to the non-functionalized FePc catalyst (+1.00134). This observation supports the proposed charge transfer from the axial ligands to the FePc site and validates the superior performance of the catalysts with axial coordination over the FePc catalyst (FePc/CNT-NH_2 > FePc/CNT-OH > FePc/CNT-COOH > FePc/CNT). Furthermore, the excellent ORR activity of the FePc/CNT-NH_2 catalyst, in comparison to the other two functionalized materials, is reflected in the more electron rich Fe site as it bears the most electron donating axial ligand donor (–NH_2 > –OH > –COOH). The enhanced ORR activity of the functionalized catalysts is further supported by the free-energy diagrams of the ORR, which were calculated according to the method of Nørskov et al.[26]

At the equilibrium potential (1.23 V), oxygen adsorption (O_2*) is downhill in the free-energy profile for all catalysts (Figure 4b). The second step, resulting in the formation of the OOH* intermediate, is uphill and the overall most endergonic step (rate determining step) of the pathway. Notably, this step is the least endergonic for the FePc/Ar–NH_2 catalyst and most endergonic for the FePc catalyst (Table S10). In the third step, the O* intermediate is formed upon the release of water, which is downhill in the free-energy profile. Similar to the adsorption of oxygen, this step is less exergonic for the catalysts with electron donating ligands coordinated. From this intermediate, another water molecule is released in two consecutive steps via the formation of the OH* intermediate. Both steps are uphill for all catalysts. However, formation of the second water molecule is overall least endergonic for the functionalized catalysts. Altogether, the free-energy pathways at the equilibrium potential reflect the experimental trends in catalytic performance.

In addition, the free-energy diagrams of ORR were calculated at 230, 330, and 630 mV overpotentials (Table S10, Figures 4c, S18, and S19). The experimental results demonstrate that at 230 mV overpotential the FePc/CNT-NH_2 catalyst starts to reduce oxygen (E_{onset} = 1.00 V), whereas the other catalysts require a slightly higher overpotential. The calculated free-energy diagram at a 230 mV overpotential reflects this, since the formation of the second water molecule becomes clearly less endergonic for the functionalized catalysts (FePc/Ar–NH_2 < FePc/Ar–OH < FePc/Ar–COOH < FePc). Furthermore, at 330 mV overpotential (E = 0.9 V, Figure S18), the formation of the second water molecule becomes downhill in the free-energy profile for the FePc/Ar–NH_2 catalyst, whereas this is still slightly uphill for the other catalysts. Only with a 630 mV overpotential (E = 0.6 V, Figure S19) or larger (Figure S20), the full free-energy profile is downhill for all catalysts investigated. Altogether, the FePc/Ar–NH_2 catalyst clearly requires the lowest overpotential, which is in accordance with the experimental results and highlights the superior performance of the FePc/CNT-NH_2 catalyst.

Conclusions

We have demonstrated that molecular iron phthalocyanine was supported on functionalized multi-walled carbon nanotubes (FePc/CNT-R, R = NH_2, COOH, or OH) to enhance its performance in the electrochemical oxygen reduction reaction (ORR). FePc/CNT-NH_2, bearing the most electron-donating axial ligand, shows an onset potential (E_{onset}) of 1.0 V and half-wave potential ($E_{1/2}$) of 0.92 V, exceeding the most advanced Fe-based ORR catalysts and also the state-of-the-art Pt/C catalyst (E_{onset} = 1.00 V and $E_{1/2}$ = 0.85 V). With help of density functional theory calculations, it has been demonstrated that the axial coordination of electron donating ligands facilitates the adsorption of oxygen, which becomes more exothermic upon coordination of more electron donating ligands. Moreover, the formation of the OOH* intermediate, which is considered the overall rate-determining step, is less endergonic for the functionalized catalysts and explains the lower overpotentials required. Altogether, this discovery demonstrates a feasible strategy to develop a series of advanced ORR catalysts that have been tailored towards sufficient oxygen adsorption and excellent ORR activity, which paves the way towards rational design of highly active electrocatalysts for other proton-coupled electron transfer reactions.

Experimental Section

Materials: All chemicals and solvents were used as received without further purification. Iron phthalocyanine (FePc, > 98 %), *N*,*N*-dimethylformamide (DMF, AR), and potassium hydroxide (KOH, AR) were purchased from Aladdin Industrial Inc. CNT and CNT-R (R = NH_2, OH and COOH) were purchased from Chengdu Zhongke Time Nano Technology Co., Ltd. Commercial Pt/C (20 wt.%) and Nafion (5 wt.%) were purchased from Suzhou Yilongsheng Energy Technology Co., Ltd.

Synthesis of FePc/CNT-R: Under ultrasonic conditions, 10 mg FePc and 40 mg CNT or CNT-R (R = NH_2, OH, and COOH) were dispersed in DMF, respectively. Subsequently, the FePc DMF solution was dropped into CNTs DMF solution under stirring. The mixed solution was sonicated for 1 h and then stirred for 24 h. Finally, the obtained solution was filtered, washed with DMF and ethanol for 3 times, and dried at 80 °C under vacuum.

Electrochemical analysis: All ORR tests were performed at the conventional three-electrode system of the CHI 760E electrochemical workstation. A glassy carbon electrode (GCE) was used as the working electrode, and a saturated calomel electrode (SCE) was used as reference electrode and Pt wire was used as counter electrode. For working electrode preparation, 4 mg of catalyst was dissolved in 1 mL of 0.2 % Nafion solution and then sonicated for 30 min to obtain a homogeneous ink. 10 μL ink was dropped on the surface of polished glassy carbon electrode and dried at 25 °C.

Electrochemical data processing: The number of electrons transferred (n) and kinetic current density (J_K) during ORR were calculated according to Koutecky–Levich Equation (1) and (2):

$$\frac{1}{J}=\frac{1}{J_L}+\frac{1}{J_K}=\frac{1}{B\omega^{1/2}}+\frac{1}{J_K} \quad (1)$$

$$B = 0.62nFC_0(D_0)^{2/3}\upsilon^{-1/6} \quad (2)$$

where J is the measured current, J_L is the diffusion-limited current densities, J_k is the kinetic-limited current densities, ω is the electrode rotation rate, n is the electron transfer number, B is the reciprocal of the slope, F is the Faraday constant (96485 C mol^{-1}), C_0 is the concentration of dissolved oxygen in electrolyte (1.2×10^{-6} mol cm^{-3}), D_0 is the diffusion coefficient of dissolved oxygen (1.9×10^{-5} $cm^2 s^{-1}$), and ν is the kinematic viscosity of the electrolyte (0.01 $cm^2 s^{-1}$).

The hydrogen peroxide yield (H_2O_2%) and the electron transfer number (n) were determined by the following Equations (3) and (4):

$$n = 4\times\frac{I_{disk}}{\frac{I_{ring}}{N}+I_{disk}} \quad (3)$$

$$H_2O_2\% = 200\times\frac{I_{ring}}{N\times I_{disk}+I_{ring}} \quad (4)$$

where I_{disk} is disk current, I_{ring} is ring current, and N is current collection efficiency of the Pt ring, which was provided as 0.37 by the manufacturer. The turnover frequency (TOF) of catalytically active Fe sites can be obtained according to Equation (5):[5a]

$$TOF = \frac{J_k N_e M_{Fe}}{\omega_{Fe} C_{cat} N_A} \quad (5)$$

where N_e is the electron number per Coulomb 6.24×10^{18}, ω_{Fe} is the active Fe content in catalysis, C_{cat} is the catalyst loading, N_A is the Avogadro constant (6.022×1023), and M_{Fe} is the molar mass of Fe (55.845 g mol^{-1}).

Acknowledgements

This work was supported by the National Natural Science Foundation of China (No. 21905073 and 22008048), Hundred Talents Project of Hebei Province (No. E2019050015), Natural Science Foundation of Hebei Province (No. B2021202010), Natural Science Foundation for Outstanding Youth Scholars of Hebei Province (No. B2021202061), the State Key Laboratory of Fine Chemicals (KF 1909), and Fundamental Research Foundation of Hebei University of Technology (JBKYTD2001). The work performed at the UvA was supported by the University of Amsterdam, which is kindly acknowledged for their financial contribution to the RPA sustainable chemistry.

Conflict of Interest

The authors declare no conflict of interest.

Data Availability Statement

The data that support the findings of this study are available in the supplementary material of this article.

Keywords: carbon nanotubes · electrocatalysis · heterogeneous catalysis · iron phthalocyanine · oxygen reduction

[1] a) S. Zaman, L. Huang, A. I. Douka, H. Yang, B. You, B. Y. Xia, *Angew. Chem. Int. Ed.* **2021**, *60*, 2–23; *Angew. Chem.* **2021**, *133*, 2–2; b) M. Shao, Q. Chang, J.-P. Dodelet, R. Chenitz, *Chem. Rev.* **2016**, *116*, 3594–3657.
[2] a) Y.-J. Wang, N. Zhao, B. Fang, H. Li, X. T. Bi, H. Wang, *Chem. Rev.* **2015**, *115*, 3433–3467; b) J. Zhang, Y. Yuan, L. Gao, G. Zeng, M. Li, H. Huang, *Adv. Mater.* **2021**, *33*, 2006494.
[3] A. A. Gewirth, J. A. Varnell, A. M. DiAscro, *Chem. Rev.* **2018**, *118*, 2313–2339.
[4] a) M. L. Pegis, C. F. Wise, D. J. Martin, J. M. Mayer, *Chem. Rev.* **2018**, *118*, 2340–2391; b) A. B. Sorokin, *Chem. Rev.* **2013**, *113*, 8152–8191; c) X. Wang, Y. Jia, X. Mao, D. Liu, W. He, J. Li, J. Liu, X. Yan, J. Chen, L. Song, A. Du, X. Yao, *Adv. Mater.* **2020**, *32*, 2000966.
[5] a) Z. Li, Z. Zhuang, F. Lv, H. Zhu, L. Zhou, M. Luo, J. Zhu, Z. Lang, S. Feng, W. Chen, L. Mai, S. Guo, *Adv. Mater.* **2018**, *30*, 1803220; b) P. Peng, L. Shi, F. Huo, C. Mi, X. Wu, S. Zhang, Z. Xiang, *Sci. Adv.* **2019**, *5*, 2322; c) J.-D. Yi, R. Xu, Q. Wu, T. Zhang, K.-T. Zang, J. Luo, Y.-L. Liang, Y.-B. Huang, R. Cao, *ACS Energy Lett.* **2018**, *3*, 883–889.
[6] a) K. Yuan, D. Luetzenkirchen-Hecht, L. Li, L. Shuai, Y. Li, R. Cao, M. Qiu, X. Zhuang, M. K. H. Leung, Y. Chen, U. Scherf, *J. Am. Chem. Soc.* **2020**, *142*, 2404–2412; b) H. Shang, X. Zhou, J. Dong, A. Li, X. Zhao, Q. Liu, Y. Lin, J. Pei, Z. Li, Z. Jiang, D. Zhou, L. Zheng, Y. Wang, J. Zhou, Z. Yang, R. Cao, R. Sarangi, T. Sun, X. Yang, X. Zheng, W. Yan, Z. Zhuang, J. Li, W. Chen, D. Wang, J. Zhang, Y. Li, *Nat. Commun.* **2020**, *11*, 3049.
[7] a) M. Che, *Catal. Today* **2013**, *218–219*, 162–171; b) T. Bligaard, J. K. Nørskov, S. Dahl, J. Matthiesen, C. H. Christensen, J. Sehested, *J. Catal.* **2004**, *224*, 206–217; c) D. Chen, L.-H. Zhang, J. Du, H. Wang, J. Guo, J. Zhan, F. Li, F. Yu, *Angew. Chem. Int. Ed.* **2021**, *60*, 24022–24027; d) J Guo, W. Zhang, L.-H. Zhang, D. Chen, J. Zhan, X. Wang, N. R. Shiju, F. Yu, *Adv. Sci.* **2021**, 2102884.

[8] a) W. Li, A. Yu, D. C. Higgins, B. G. Llanos, Z. Chen, *J. Am. Chem. Soc.* **2010**, *132*, 17056–17058; b) X. Yu, S. Lai, S. Xin, S. Chen, X. Zhang, X. She, T. Zhan, X. Zhao, D. Yang, *Appl. Catal. B* **2021**, *280*, 119437.
[9] a) H. Michel, J. Behr, A. Harrenga, A. Kannt, *Annu. Rev. Biophys. Biomol. Struct.* **1998**, *27*, 329–356; b) X. Huang, J. T. Groves, *Chem. Rev.* **2018**, *118*, 2491–2553.
[10] J. P. Collman, N. K. Devaraj, R. A. Decréau, Y. Yang, Y.-L. Yan, W. Ebina, T. A. Eberspacher, C. E. D. Chidsey, *Science* **2007**, *315*, 1565.
[11] a) W. Zhang, W. Lai, R. Cao, *Chem. Rev.* **2017**, *117*, 3717–3797; b) L. Xie, X.-P. Zhang, B. Zhao, P. Li, J. Qi, X. Guo, B. Wang, H. Lei, W. Zhang, U.-P. Apfel, R. Cao, *Angew. Chem. Int. Ed.* **2021**, *60*, 7576–7581.
[12] a) L.-H. Zhang, S. Mathew, J. Hessels, J. N. H. Reek, F. Yu, *ChemSusChem* **2021**, *14*, 234–250; b) D. J. Wasylenko, C. Rodríguez, M. L. Pegis, J. M. Mayer, *J. Am. Chem. Soc.* **2014**, *136*, 12544–12547; c) A. Hosseini, C. J. Barile, A. Devadoss, T. A. Eberspacher, R. A. Decreau, J. P. Collman, *J. Am. Chem. Soc.* **2011**, *133*, 11100–11102; d) C. T. Carver, B. D. Matson, J. M. Mayer, *J. Am. Chem. Soc.* **2012**, *134*, 5444–5447; e) M. L. Rigsby, D. J. Wasylenko, M. L. Pegis, J. M. Mayer, *J. Am. Chem. Soc.* **2015**, *137*, 4296–4299; f) J. B. Jakobsen, M. H. Rønne, K. Daasbjerg, T. Skrydstrup, *Angew. Chem. Int. Ed.* **2021**, *60*, 9174–9179; g) J. Meng, H. Lei, X. Li, W. Zhang, R. Cao, *J. Phys. Chem. C* **2020**, *124*, 16324–16331.
[13] K. Chen, K. Liu, P. An, H. Li, Y. Lin, J. Hu, C. Jia, J. Fu, H. Li, H. Liu, Z. Lin, W. Li, J. Li, Y.-R. Lu, T.-S. Chan, N. Zhang, M. Liu, *Nat. Commun.* **2020**, *11*, 4173.
[14] a) W. Zhang, S. Yang, S.-T. Bai, L.-H. Zhang, Y. Zhang, F. Yu, *ChemCatChem* **2021**, *13*, 1546–1551; b) L. Xie, X. Li, B. Wang, J. Meng, H. Lei, W. Zhang, R. Cao, *Angew. Chem. Int. Ed.* **2019**, *58*, 18883–18887; *Angew. Chem.* **2019**, *131*, 19059–19063; c) X. Li, H. Lei, J. Liu, X. Zhao, S. Ding, Z. Zhang, X. Tao, W. Zhang, W. Wang, X. Zheng, R. Cao, *Angew. Chem. Int. Ed.* **2018**, *57*, 15070–15075; *Angew. Chem.* **2018**, *130*, 15290–15295; d) H. Lei, C. Liu, Z. Wang, Z. Zhang, M. Zhang, X. Chang, W. Zhang, R. Cao, *ACS Catal.* **2016**, *6*, 6429–6437.
[15] R. Cao, R. Thapa, H. Kim, X. Xu, M. Gyu Kim, Q. Li, N. Park, M. Liu, J. Cho, *Nat. Commun.* **2013**, *4*, 2076.
[16] a) Z. Chen, A. Huang, K. Yu, T. Cui, Z. Zhuang, S. Liu, J. Li, R. Tu, K. Sun, X. Tan, J. Zhang, D. Liu, Y. Zhang, P. Jiang, Y. Pan, C. Chen, Q. Peng, Y. Li, *Energy Environ. Sci.* **2021**, *14*, 3430–3437; b) A. Pizarro, G. Abarca, C. Gutiérrez-Cerón, D. Cortés-Arriagada, F. Bernardi, C. Berrios, J. F. Silva, M. C. Rezende, J. H. Zagal, R. Oñate, I. Ponce, *ACS Catal.* **2018**, *8*, 8406–8419.
[17] a) P. Tian, B. Zhang, J. Chen, J. Zhang, L. Huang, R. Ye, B. Bao, M. Zhu, *Catal. Sci. Technol.* **2021**, *11*, 2491–2496; b) F. Li, B. Zhang, X. Li, Y. Jiang, L. Chen, Y. Li, L. Sun, *Angew. Chem. Int. Ed.* **2011**, *50*, 12276–12279; *Angew. Chem.* **2011**, *123*, 12484–12487.
[18] F. Xu, L. Zhang, X. Ding, M. Cong, Y. Jin, L. Chen, Y. Gao, *Chem. Commun.* **2019**, *55*, 14111–14114.
[19] W. Liu, L. Zhang, X. Liu, X. Liu, X. Yang, S. Miao, W. Wang, A. Wang, T. Zhang, *J. Am. Chem. Soc.* **2017**, *139*, 10790–10798.
[20] Y. Pan, R. Lin, Y. Chen, S. Liu, W. Zhu, X. Cao, W. Chen, K. Wu, W.-C. Cheong, Y. Wang, L. Zheng, J. Luo, Y. Lin, Y. Liu, C. Liu, J. Li, Q. Lu, X. Chen, D. Wang, Q. Peng, C. Chen, Y. Li, *J. Am. Chem. Soc.* **2018**, *140*, 4218–4221.
[21] W. Cheng, P. Yuan, Z. Lv, Y. Guo, Y. Qiao, X. Xue, X. Liu, W. Bai, K. Wang, Q. Xu, J. Zhang, *Appl. Catal. B* **2020**, *260*, 118198.
[22] D. Guo, R. Shibuya, C. Akiba, S. Saji, T. Kondo, J. Nakamura, *Science* **2016**, *351*, 361–365.
[23] a) X. Li, C.-S. Cao, S.-F. Hung, Y.-R. Lu, W. Cai, A. I. Rykov, S. Miao, S. Xi, H. Yang, Z. Hu, J. Wang, J. Zhao, E. E. Alp, W. Xu, T.-S. Chan, H. Chen, Q. Xiong, H. Xiao, Y. Huang, J. Li, T. Zhang, B. Liu, *Chem* **2020**, *6*, 3440–3454; b) Z. Zhang, M. Dou, J. Ji, F. Wang, *Nano Energy* **2017**, *34*, 338–343; c) P. Chen, T. Zhou, L. Xing, K. Xu, Y. Tong, H. Xie, L. Zhang, W. Yan, W. Chu, C. Wu, Y. Xie, *Angew. Chem. Int. Ed.* **2017**, *56*, 610–614; *Angew. Chem.* **2017**, *129*, 625–629; d) Z. Zhang, J. Sun, F. Wang, L. Dai, *Angew. Chem. Int. Ed.* **2018**, *57*, 9038–9043; *Angew. Chem.* **2018**, *130*, 9176–9181; e) J. Zhang, Y. Zhao, C. Chen, Y.-C. Huang, C.-L. Dong, C.-J. Chen, R.-S. Liu, C. Wang, K. Yan, Y. Li, G. Wang, *J. Am. Chem. Soc.* **2019**, *141*, 20118–20126.
[24] T. Wang, X. Cao, H. Qin, L. Shang, S. Zheng, F. Fang, L. Jiao, *Angew. Chem. Int. Ed.* **2021**, *60*, 21237–21241.
[25] A. E. Reed, R. B. Weinstock, F. Weinhold, *J. Chem. Phys.* **1985**, *83*, 735–746.
[26] J. K. Nørskov, J. Rossmeisl, A. Logadottir, L. Lindqvist, J. R. Kitchin, T. Bligaard, H. Jónsson, *J. Phys. Chem. B* **2004**, *108*, 17886–17892.

Manuscript received: November 8, 2021
Revised manuscript received: December 7, 2021
Accepted manuscript online: December 14, 2021
Version of record online: January 10, 2022